Ab Initio QM/MM Molecular Dynamics Study on the Excited-State Hydrogen Transfer of 7-Azaindole in Water Solution

Daisuke Kina, Akira Nakayama, Takeshi Noro, and Tetsuya Taketsugu*

Division of Chemistry, Graduate School of Science, Hokkaido University, Sapporo 060-0810, Japan

Mark S. Gordon

Department of Chemistry, Iowa State University, Ames, Iowa 50011

Received: May 17, 2008; Revised Manuscript Received: July 16, 2008

Ab initio molecular dynamics (AIMD) simulations for the excited-state hydrogen transfer (ESHT) reaction of 7-azaindole (7AI−$(H_2O)_n$; $n = 1, 2$) clusters in the gas phase and in water are presented. The effective fragment potential (EFP) is employed to model the surrounding water molecules. The AIMD simulations for 7AI−H_2O and 7AI−$(H_2O)_2$ clusters show an asynchronous hydrogen transfer at $t \sim 50$ fs after the photoexcitation. While the ESHT mechanism for 7AI−H_2O in water does not change appreciably compared with that in the gas phase, the AIMD simulations on 7AI−$(H_2O)_2$ in water solution exhibit two different mechanisms. Since the tautomer form is lower in energy compared to the normal form in the S_1 state, 7AI and $(H_2O)_n$ fragments separate from each other after the ESHT. With the use of the results of the AIMD trajectories, the minimum energy conical intersection point in the tautomer region has also been located.

I. Introduction

Excited-state hydrogen transfer (ESHT) is a fundamental reaction which plays an important role in a variety of biological processes.[1−3] Typically, this type of transfer occurs through a hydrogen-bonded network. 7-Azaindole (7AI) is a molecule in which this process is important. Tautomerization of 7AI, accompanying the ESHT from the five-membered ring to the six-membered ring, has been studied with much attention both experimentally[4−21] and theoretically,[22−30] since 7AI can be regarded as a simple model for DNA base pairs. Very recently, Sakota and co-workers measured the dispersed fluorescence (DF) spectra and resonance-enhanced multiphoton ionization (REMPI) spectra for the 7AI−$(H_2O)_n$ ($n = 2, 3$) cluster at low temperature in the gas phase and found that the tautomerization of 7AI−$(H_2O)_n$ ($n = 2, 3$) occurs in the S_1 state,[21] although it was not observed at first based on the measurement of the fluorescence excitation (FE) and DF spectra.[16] It was also reported[18,19] by the same group that the excited-state triple-H-transfer occurs in the 7AI−$(MeOH)_2$ cluster, based on the measurement of DF and REMPI spectra, but the tautomerization does not occur in 7AI−MeOH and 7AI−$(MeOH)_3$ clusters. They pointed out that ESHT in 7AI−$(MeOH)_2$ proceeds via a tunneling mechanism in their experimental conditions, and the excitation of the low-energy intermolecular stretching mode accelerates ESHT in 7AI−$(MeOH)_2$.

An early theoretical effort on the ESHT reaction of 7AI−H_2O was performed by Chaban and Gordon,[22,24] in which the intrinsic reaction coordinate was calculated for the tautomerization in an isolated 7AI molecule and the 7AI−H_2O complex in the singlet ground (S_0) and first excited (S_1) states at the CASSCF (complete active space self-consistent field) level of theory, with improved energetics obtained using multireference second-order perturbation theory (MCQDPT2).[31] It was shown that the normal form of 7AI is more stable than the tautomer in the S_0 state, whereas the relative energies are reversed in the S_1 state. The activation energy for tautomerization in 7AI is significantly reduced by the complexation with water, because then the H transfer occurs via the 7AI−H_2O hydrogen-bonded network. Casadesús et al.[27] examined the reaction profile for the tautomerization of 7AI−$(H_2O)_n$ ($n = 0−4$) in the S_1 state using single-excitation configuration interaction (CIS) geometry optimization, followed by time-dependent density functional theory (TDDFT) energy calculations, and discussed the dependence of the activation barriers on the number of attached water molecules. They found that the ESHT mechanism in 7AI−$(H_2O)_2$ is the most efficient one among 7AI−$(H_2O)_n$ ($n = 0−4$) clusters.

In addition to the experimental observation in the gas phase, the tautomerization in 7AI was also observed in the condensed phase in alcohol or water solution,[4−10,12] where the tautomerization exhibits a strong dependence on the water concentration in mixtures of water and aprotic solvents.[8] It is possible that ESHT would exhibit different mechanisms for the reactions in the gas phase and in the condensed phase. The spectroscopic experiments in the gas phase have been carried out at very low temperature, and so quantum mechanical tunneling could contribute significantly to the ESHT reaction. On the other hand, the experiments in solution have been carried out at room temperature, and ESHT reactions could occur classically (without tunneling), because there is sufficient energy in the system to overcome the small activation barrier. Fernández-Ramos et al.[26] calculated the rate constant for the ESHT reaction of 7AI in solution using the Onsager model. Although the rate constants calculated for 7AI−H_2O and 7AI−$(H_2O)_2$ embedded in a dielectric continuum did not reproduce the experimental ones in dilute solution, those calculated for the 7AI−$(H_2O)_5$ complex were shown to reproduce the observed order of magnitude.

* To whom correspondence should be addressed. Fax: +81-11-706-4921. E-mail: take@sci.hokudai.ac.jp.

10.1021/jp804368p CCC: $40.75
Published on Web 09/11/2008

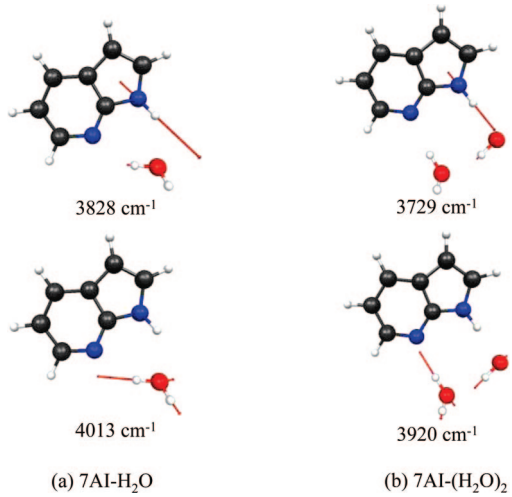

Figure 1. Two normal modes of vibration related to the reaction coordinate of the ESHT for (a) 7AI−H_2O and (b) 7AI−$(H_2O)_2$.

The Onsager model has limited accuracy for predicting solvent effects and cannot account for explicit solute−solvent interactions, so a more sophisticated approach would be useful for improving the understanding of the effects of solvation structures on the dynamics. One alternative approach is the effective fragment potential (EFP) method,[32,33] implemented in the program package GAMESS,[34,35] in which each solvent molecule is represented by a discrete model potential. When combined with an electronic structure calculation for the solute, this method can be classified as a quantum mechanics combined with molecular mechanics (QM/MM) approach. The solvent molecules that participate directly in the reaction process should be included in the QM part, while the environmental solvent molecules can be represented by EFPs. In this work, we present ab initio QM/MM molecular dynamics (AIMD) simulations for the excited-state full tautomerization process in 7AI−$(H_2O)_n$ (n = 1, 2) clusters in a water solvent environment and investigate the role of solvent water molecules on the ESHT reaction. The AIMD method is based on a classical trajectory, in which the force acting on each atom is calculated "on-the-fly" by ab initio calculations,[36,37] and it has been extended to excited-state dynamics very recently,[38,39] including a nonadiabatic surface-hopping scheme.[40]

II. Computational Details

Geometry optimizations and normal-mode analyses were carried out for 7AI and 7AI−$(H_2O)_n$ (n = 1, 2) in the ground and first excited singlet states by the state-specific CASSCF method with the segmented DZP basis set,[41−43] using the quantum chemical program package, GAMESS.[34,35] The CASSCF active space includes 10 electrons in 9 orbitals which comprise all of the 7AI π orbitals and electrons. The transition state geometries for tautomerization in 7AI−H_2O and 7AI−$(H_2O)_2$ were determined by the same methods. Following the examination of the energetics of the reactions, AIMD simulations were performed for the ESHT processes in 7AI−$(H_2O)_n$ (n = 1, 2). The AIMD code used here is based on the leapfrog algorithm[44] and utilizes ab initio energy gradients. The initial conditions for the dynamics simulations were the equilibrium structures in the ground state, with the atomic velocities given in the directions of the H transfer. The latter consists of two normal modes, shown in Figure 1 (plotted with MacMolPlt[45]). Preliminary AIMD simulations were performed in which the vibrational quantum numbers were successively incremented by one. It was determined that at least a vibrational energy equivalent to three photons is required to invoke H-transfer reactions within a tractable amount of time. Therefore, the kinetic energy given to the respective modes in the production simulations corresponds to three photons. These initial conditions were employed to promote the H transfer efficiently.

To simulate the ESHT processes in water, 100 Hartree−Fock (HF)-based effective fragment potential (EFP1/HF) water molecules were distributed around 7AI−$(H_2O)_n$. The EFP1/HF method was developed to describe water clusters, either with or without an explicit ab initio solute system.[32,33] The method accounts for three important interaction terms: (a) Coulomb interactions for solute−solvent and solvent−solvent, (b) solute−solvent and solvent−solvent polarization interactions, and (c) exchange repulsion + charge transfer interactions. In the presence of an ab initio solute, these terms are added as one-electron terms to the ab initio Hamiltonian. The Coulomb interaction term is approximated with a distributed multipolar analysis (DMA) of the solvent molecule, expanded through octopoles. The polarization term is treated by a self-consistent distributed perturbation model with localized molecular orbital (LMO) polarizability tensors. In order to obtain the remaining (exchange repulsion + charge transfer) interaction, the first two terms are calculated for many points on the water dimer potential energy surface and subtracted from the total Hartree−Fock interaction potential. This remainder (exchange repulsion + charge transfer) interaction is then fitted to a functional form.[32,33] Note that the internal geometry of an EFP water is fixed.

The AIMD simulations for an ab initio solute in the excited state surrounded by EFP solvent molecules require analytic energy gradients for both the ab initio and EFP parts. In the current version of GAMESS, such excited-state simulations can only be performed with state-specific CASSCF.[46] The electron density used to determine induced dipoles in EFP is obtained from the orbitals and CI coefficients of the selected CASSCF state. That is, the density in the MO basis is formed from the CI coefficients of the chosen state and then transformed to the AO basis via the MO coefficients; the resulting AO density matrix is then used for the polarization step (this is performed in each CASSCF iteration until self-consistency is attained).

The RHF/STO-3G-AIMD simulations for 7AI−$(H_2O)_n$−EFP were performed in the ground state for 10 ps at a constant temperature of 300 K with a time step of 1 fs. In this process the geometry of the solute 7AI−$(H_2O)_n$ was fixed. Twenty different configurations and velocities of EFPs were chosen from the above AIMD trajectories and used as the initial conditions for the AIMD simulations in the excited state. The AIMD simulations for phototautomerizations in 7AI−$(H_2O)_n$ and 7AI−$(H_2O)_n$−EFP (n = 1, 2) were performed at the CASSCF level of theory with the segmented DZP basis set, and the solvent effects on the ESHT processes were investigated from the dynamical point of view. The time step was taken as 0.5 fs throughout the simulation.

The minimum energy conical intersection point for the S_0 and S_1 states was also located, with the state-averaged CASSCF (SA-CASSCF) method in the Molpro program.[47] The role of this conical intersection in the ESHT process is discussed, based on the results of the AIMD simulations. To estimate more accurate energetics for the reactions, CASPT2 calculations[48] were also carried out in the S_0 and S_1 states.

III. Results and Discussion

III.A. Energetics and Dynamics of Tautomerization in the 7AI−$(H_2O)_n$ Cluster. Figure 2 shows the calculated equilibrium geometries for the normal and tautomer forms of 7AI−H_2O and

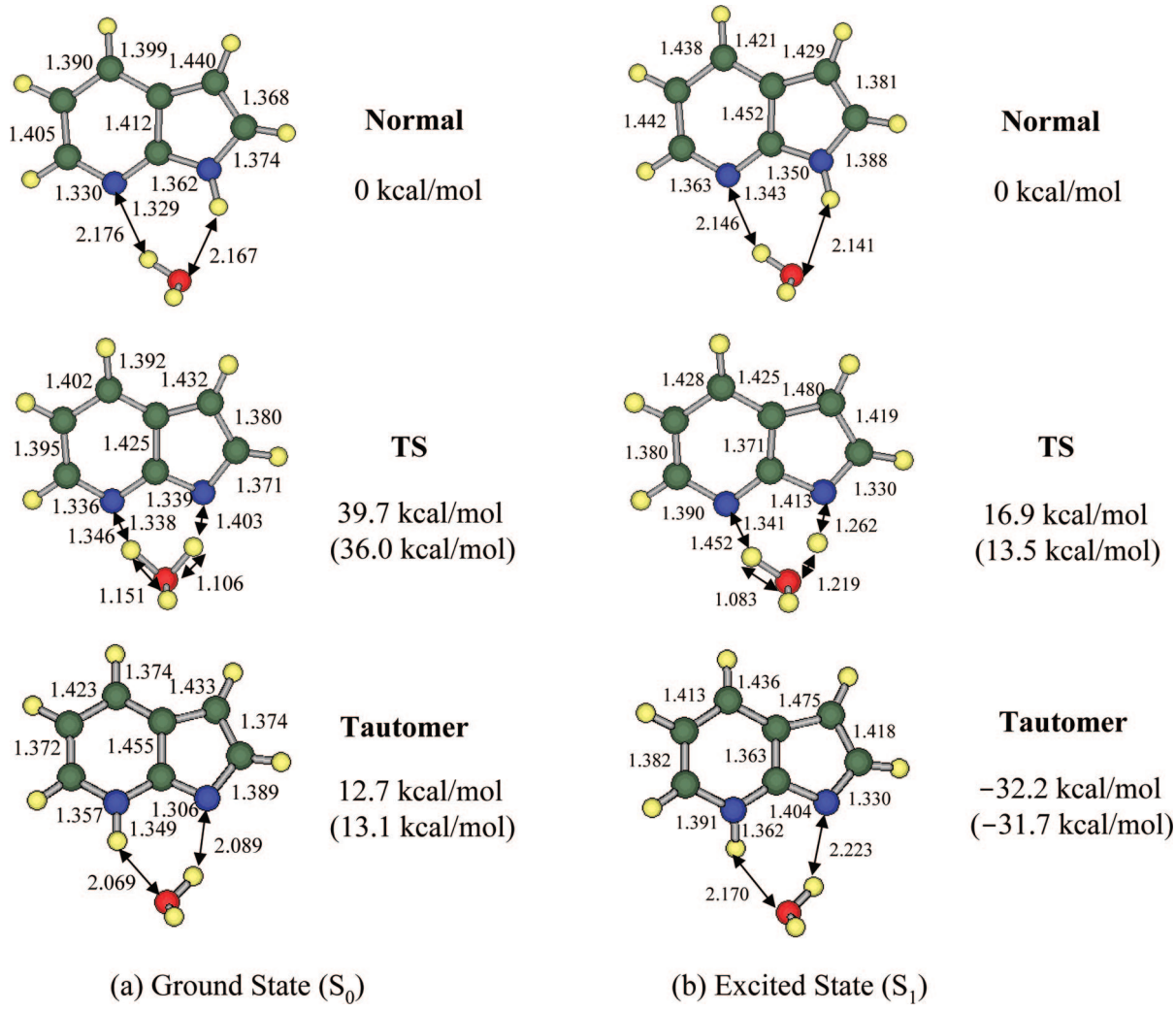

Figure 2. Equilibrium geometries of the normal form, tautomer form, and the transition state (TS) in the S_0 and S_1 states of 7AI−H_2O. Interatomic distances are given in angstroms. Relative CASSCF energies are also shown, where the numbers in parentheses are vibrational zero-point corrected values.

the transition state (TS) geometries for tautomerization in both the S_0 and S_1 states, where the CASSCF interatomic distances and relative energies are given. In the transition states, double-H-transfer occurs in a concerted manner in both the S_0 and S_1 states. Each transition state has only one imaginary frequency. When the S_0 and S_1 equilibrium structures are compared, it is observed that most CC and CN bond distances increase upon photoexcitation. This feature is related to the character of the CASSCF wave function in the S_1 state, in which several electronic configurations with excitations from π to π^* orbitals contribute to the S_1 wave function. As a result, vibrational excitation of the 7AI ring-skeleton may be induced by the photoexcitation. The normal form is lower in energy by ca. 13 kcal/mol than the tautomer in the S_0 state, whereas the tautomer is lower in energy by ca. 32 kcal/mol than the normal form in the S_1 state. The activation barriers relative to the normal isomer are 39.7 and 16.9 kcal/mol, respectively, in the S_0 and S_1 states (the vibrational zero-point corrected barriers are 36.0 and 13.5 kcal/mol), so the H-transfer reaction occurs more easily in the S_1 state. The geometries and relative energies are in good agreement with those reported by Chaban and Gordon;[24] the differences in the interatomic distances and relative energies are ∼0.025 Å and 1.3 kcal/mol, respectively, except for the TS geometry in the S_0 state. The difference in this TS geometry is caused by the use of different basis sets. The energy profiles for the tautomerization in 7AI−$(H_2O)_2$ are almost the same as those in 7AI−H_2O. As will be discussed later, it is found that inclusion of dynamic electron correlation by CASPT2 lowers the activation energy in both the S_0 and S_1 states (see Table 1).

The AIMD trajectory simulations were started on the S_1 excited state from the ground-state equilibrium structure for the normal form of 7AI−$(H_2O)_n$. The initial velocities are given in the directions of the H transfer consisting of the two normal modes shown in Figure 1, whose frequencies are 3828 and 4013 cm^{-1} for 7AI−H_2O and 3729 and 3920 cm^{-1} for 7AI−$(H_2O)_2$, respectively. The kinetic energy is given to the respective modes with three quanta, and this amounts to 67.3 and 65.6 kcal/mol for 7AI−H_2O and 7AI−$(H_2O)_2$, respectively. Figure 3 displays the time evolution of (a) the relative energy between the S_0 and S_1 states and (b) the interatomic distances related to the H transfer along the AIMD trajectory for 7AI−H_2O. During the initial 40 fs, the molecule stays in the normal-form region of the potential energy surface, with fluctuations in the excitation energy with a period of ∼10 fs (Figure 3a); this is consistent with the approximate period of vibration of the N···H and O···H hydrogen-bond stretching modes as shown in Figure 3b. The excitation energy in Figure 3a decreases rapidly at ∼50 fs, and the hydrogen-bond distances, N···H and O···H, decrease to covalent bond lengths, indicating that ESHT occurs through the hydrogen-bonded network. The N···H and O···H hydrogen-

TABLE 1: Relative Energies (kcal/mol) for Points Related to the H-Transfer Reactions in the S_0 and S_1 States for 7AI, 7AI−H_2O, and 7AI−$(H_2O)_2$ Calculated with SA-CASSCF and CASPT2

	normal			tautomer		
	S_0-min	S_1-min	TS	S_0-min	S_1-min	MECI[a]
			7AI			
SA-CASSCF						
S_0	0.0	4.8	85.8	16.5	33.1	
S_1	111.1	106.3	168.5	92.6	75.3	88.0
CASPT2						
S_0	0.0	1.3	61.1	13.0	22.3	
S_1	104.8	98.0	138.6	85.3	71.9	98.8
			7AI−H_2O			
SA-CASSCF						
S_0	0.0	4.7	42.5	14.3	30.6	
S_1	110.5	105.8	127.0	92.4	76.3	
CASPT2						
S_0	0.0	1.1	19.4	9.9	20.0	
S_1	103.5	96.7	99.2	85.0	72.9	
			7AI−$(H_2O)_2$			
SA-CASSCF						
S_0	0.0	4.6	40.9	13.3	29.7	
S_1	110.2	105.6	126.7	92.6	77.0	
CASPT2						
S_0	0.0	1.1	21.0	8.7	19.4	
S_1	102.9	96.2	100.7	85.3	73.8	

[a] Minimum energy conical intersection point.

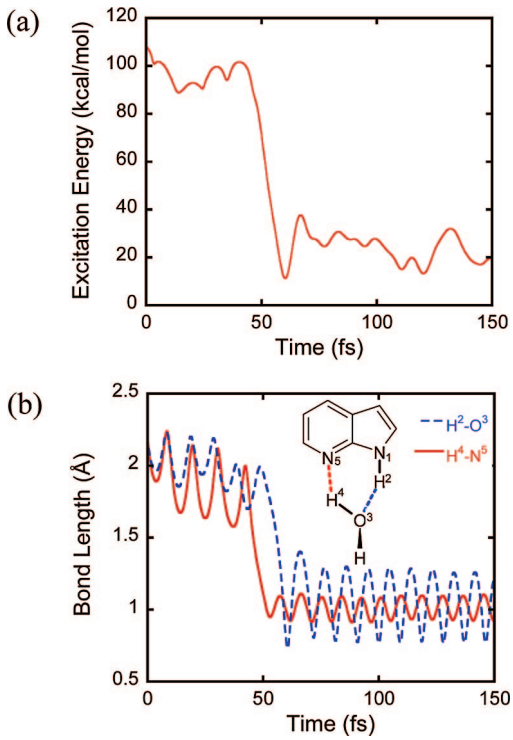

Figure 3. Time evolution of (a) the relative energy of S_0 and S_1 states and (b) the interatomic distances related to the H transfer in the AIMD simulation for 7AI−H_2O. Solid and dashed lines denote changes in the $N^5\cdots H^4$ and $O^3\cdots H^2$ distances, respectively.

bond lengths initially exhibit in-phase vibrational motions, but their relative phases gradually change, and just before the H transfer at $t = 40$ fs, they become completely out-of-phase, indicating an asynchronous H transfer. The H is transferred from H_2O to 7AI via the N···H hydrogen bond, resulting in 7AI−$H^{\delta+}\cdots OH^{\delta-}$ around $t = 50$ fs. The sum of Mulliken net atomic charges on OH is −0.67. The net charge on OH is −0.49 using charges based on the more reliable electrostatic potential fitting (ESP) method.[49,50] So, the transferring H carries a significant positive charge, but it is not a true proton transfer. Following this process, the second H transfer occurs promptly from the NH on the five-membered ring to OH, completing the tautomerization of 7AI. After the H transfer, the molecular system acquires considerable energy due to the stabilization of the tautomer in the S_1 state, and the 7AI and H_2O fragments separate, breaking the two hydrogen bonds. This dynamical behavior indicates that the ESHT reaction in 7AI−H_2O proceeds in a concerted manner via the TS structure shown in Figure 2, but rather asynchronously.

It is interesting to note the recent experimental study of Takeuchi and Tahara[20] for the double-proton-transfer in the 7AI dimer in solution, in which the 7AI dimer converts to the tautomer configuration in the excited state. They investigated this process by excitation wavelength dependence in steady-state and femtosecond time-resolved fluorescence spectroscopy and concluded that it proceeds in a concerted manner. They noted, however, that this conclusion does not necessarily translate to a synchronous motion of the two protons. A concerted mechanism does not imply strict simultaneity, only that the motions of the two protons are correlated. Ushiyama and Takatsuka[51] performed AIMD simulations for the double-H-transfer in formic acid dimer in the ground state. The minimum energy path for this process indicates that the synchronous H transfer is more favorable than the asynchronous one, but AIMD simulations showed that there is a certain time lag (∼8 fs) between the two H transfers. This type of motion is an example of a concerted double-H-transfer, which is fundamentally different from the stepwise process.

Figure 4 shows the time evolution of (a) the relative energy of the S_0 and S_1 states and (b) the interatomic distances $H^2\cdots O^3$, $H^4\cdots O^5$, and $H^6\cdots N^7$ along the 7AI$\cdots(H_2O)_2$ AIMD trajectory. Changes in the interatomic distances (Figure 4b) indicate that the triple-H-transfer relays occur in the time range of $t = 40$ to 60 fs, accompanying the gradual decrease in the excitation energy as shown in Figure 4a. A detailed picture of this process is summarized in the following three steps, i.e., (1) H^2 moves from N^1 to O^3, (2) H^4 moves from O^3 to O^5, and (3) H^6 moves from O^5 to N^7 (the tautomerization completes). In the first step, the sum of the net atomic charges on the H_5O_2 moiety is +0.58 and +0.50 according to the Mulliken and ESP population analyses, respectively. The reaction mechanism is a concerted asynchronous process. As illustrated for the 7AI−H_2O MD simulation, 7AI and H_2O fragments separate after the ESHT reaction.

As is shown in Figure 4c, the adiabatic energies of the S_0 and S_1 states approach each other in the tautomer region (indicated by arrows in the figure), suggesting the possibility of a nonradiative decay through a conical intersection of the potential energy surfaces. In order to examine this possibility, an SA-CASSCF geometry optimization was performed to determine the minimum energy conical intersection (MECI) point between the S_0 and S_1 states for an isolated 7AI molecule, starting from the structure with the smallest relative energy on the 7AI−$(H_2O)_2$ AIMD trajectory. Note that the AIMD simulations were carried out using the state-specific CASSCF method. The energetics obtained using the state-specific and state-averaged CASSCF calculations are slightly different from each other. Figure 5a shows two geometrical structures. On the left is the starting structure in the search for the MECI. On the right is the MECI structure, in which the participating H atom attached to the six-membered ring is out of the molecular plane.

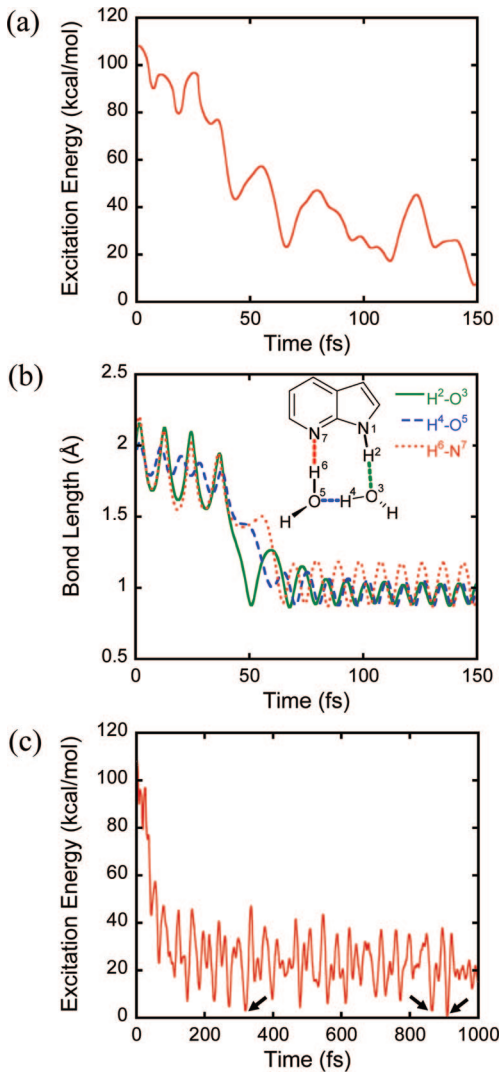

Figure 4. Time evolution of (a) the relative energy of S_0 and S_1 states and (b) the interatomic distances related to the H transfer in the AIMD simulation for 7AI−$(H_2O)_2$ where solid, dashed, and dotted lines denote changes of the $H^2\cdots O^3$, $H^4\cdots O^5$, and $H^6\cdots N^7$ distances, respectively. A longer time evolution of the relative energy of S_0 and S_1 states for 1000 fs is given in (c).

The SA-CASSCF energies for the S_1 state were calculated at linearly interpolated points between these two structures and verified that no obstructive barrier exists along the interpolated path. Therefore, when an H is transferred from the out-of-plane side to the six-membered ring N atom, 7AI could easily reach this conical intersection point, suggesting a nonradiative decay process after the phototautomerization in the 7AI−$(H_2O)_n$ (n = 1, 2) cluster.

The SA-CASSCF energies do not include dynamic electron correlation, so CASPT2[48] calculations were carried out to examine the energetics of the reactions for 7AI−H_2O and 7AI−$(H_2O)_2$. For comparison, an SA-CASSCF geometry optimization was also carried out for an isolated 7AI molecule to locate the corresponding minima and transition state on the S_0 and S_1 surfaces and performed the following CASPT2 energy calculations. Table 1 summarizes the SA-CASSCF and CASPT2 energies at significant points for 7AI, 7AI−H_2O, and 7AI−$(H_2O)_2$ on the SA-CASSCF potential energy surfaces, where S_0-min and S_1-min denote the minimum energy structures on the respective potential energy surfaces. For the MECI of S_0 and S_1 surfaces, however, geometries are determined at the respective SA-CASSCF and CASPT2 computational levels. The geometry at the MECI point on the CASPT2 potential energy surface was determined by utilizing the SA-CASSCF analytical energy gradients and the CASPT2 energy difference, assuming that the SA-CASSCF potential energy surface is parallel to the CASPT2 one. Of course the CASPT2 energy gradients are not strictly equal to the SA-CASSCF energy gradients, but the CASPT2 MECI point was located to within 0.2 kcal/mol by several trial calculations. The CASPT2 MECI geometry is shown in Figure 5b, which is very close to the SA-CASSCF MECI geometry.

As indicated already, the energy profiles for the tautomerization in 7AI−$(H_2O)_2$ are almost the same as those in 7AI−H_2O as shown in Table 1. Also, the activation barrier for tautomerization in an isolated 7AI molecule is much higher than that in 7AI−H_2O since, without a bridge of water molecules, an H needs to be directly transferred from the five-membered ring N atom to the six-membered ring N atom.[24] Note (Table 1) that the addition of dynamic correlation via CASPT2 significantly reduces the activation barrier for the reaction in both the S_0 and S_1 states. In particular, the CASPT2 activation barrier for 7AI−H_2O in the S_1 state is predicted to be only 2.5 kcal/mol at the SA-CASSCF geometries. This trend was previously pointed out by Chaban and Gordon.[24] This small activation barrier indicates that at room or higher temperatures, the H-transfer reaction does not require quantum tunneling to proceed.

III.B. Solvent Effects on the ESHT Dynamics for the 7AI−$(H_2O)_n$−EFP System. Now, consider aqueous solvation effects on the ESHT dynamics of 7AI−H_2O and 7AI−$(H_2O)_2$, using the EFP method. The accuracy of the EFP method was evaluated by comparing the hydrogen-bond distance and the binding energy of an EFP water to the 7AI−$(H_2O)_n$ clusters with those obtained by fully ab initio calculations. CASSCF calculations were performed for the 7AI−$(H_2O)_n$ (n = 1, 2) clusters with one solvent water molecule (using an EFP or an ab initio water) shown in Figure 6. The EFP hydrogen-bond distances are r_1 = 2.037 Å, r_2 = 2.191 Å, and r_3 = 2.545 Å in the S_0 state, whereas r_1 = 2.036 Å, r_2 = 2.192 Å, and r_3 = 2.555 Å in the S_1 state. The corresponding ab initio bond distances are r_1 = 2.073 Å, r_2 = 2.154 Å, and r_3 = 2.476 Å in the S_0 state and r_1 = 2.072 Å, r_2 = 2.152 Å, and r_3 = 2.489 Å in the S_1 state. The binding energy comparison was performed for the EFP-optimized structures. For the 7AI−H_2O−H_2O complex, the binding energy is 4.7 (EFP) and 5.0 kcal/mol (ab initio) in the S_0 state and 4.7 (EFP) and 5.0 kcal/mol (ab initio) in S_1. For the 7AI−$(H_2O)_2$−H_2O complex, the binding energy is 6.0 (EFP) and 6.7 kcal/mol (ab initio) in the S_0 state and 6.0 (EFP) and 6.80 kcal/mol (ab initio) in S_1. Note that the ab initio binding energies may suffer from the basis set superposition error, whereas this is not relevant for the EFP model potential. The agreement between the ab initio and EFP results are reasonable, indicating that the EFP approach is suitable for the present system.

To determine the initial positions and velocities of 100 EFP waters for the examination of excited-state dynamics, preliminary RHF AIMD simulations were carried out for the 7AI−$(H_2O)_n$−EFP (n = 1, 2) ground state. In this simulation, velocity scaling was applied for a time interval of 0.25 ps, to control the temperature of EFP waters at 300 K. The temperature shows a small fluctuation around 300 K for t > 1.0 ps. Twenty points from the trajectory were chosen as the initial conditions for the excited-state AIMD simulations. During the simulations, each EFP water maintains a hydrogen bond with other EFP or

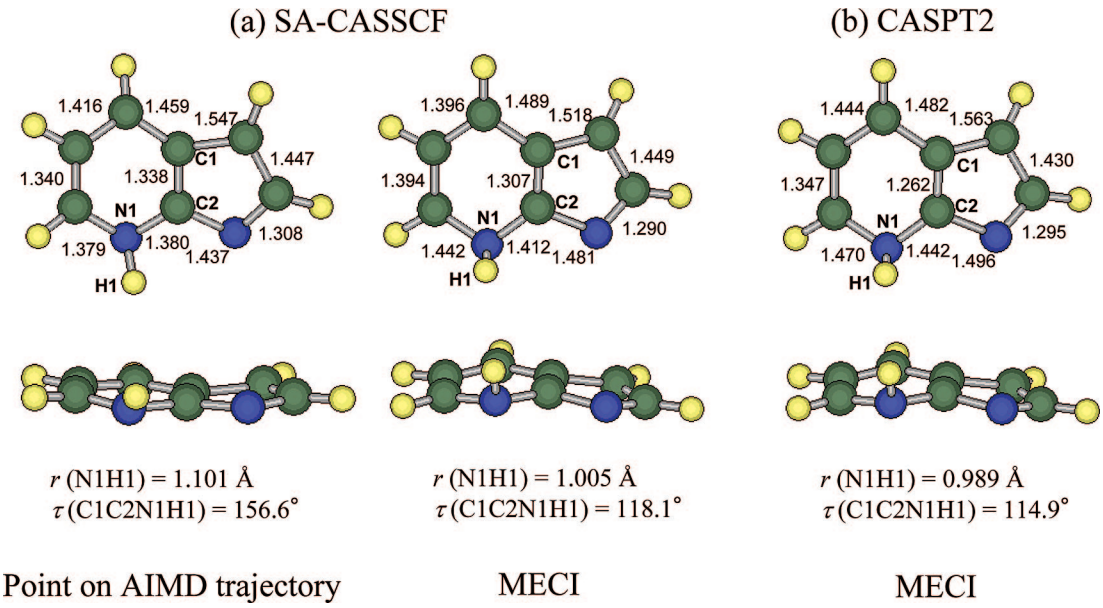

Figure 5. (a) Geometries of 7AI at the smallest excitation energy on the AIMD for 7AI−$(H_2O)_2$ and the minimum energy conical intersection (MECI) point at the SA-CASSCF level; (b) the minimum energy conical intersection point at the CASPT2 level.

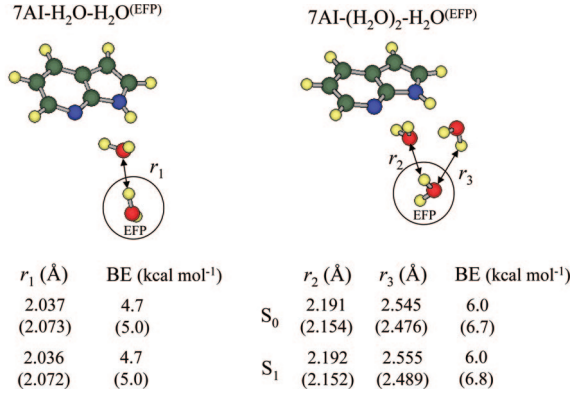

	r_1 (Å)	BE (kcal mol^{-1})		r_2 (Å)	r_3 (Å)	BE (kcal mol^{-1})
S_0	2.037 (2.073)	4.7 (5.0)	S_0	2.191 (2.154)	2.545 (2.476)	6.0 (6.7)
S_1	2.036 (2.072)	4.7 (5.0)	S_1	2.192 (2.152)	2.555 (2.489)	6.0 (6.8)

Figure 6. Geometries and binding energies of 7AI−H_2O−H_2O and 7AI−$(H_2O)_2$−H_2O for which EFP results are compared with ab initio results. The numbers in parentheses denote ab initio values.

ab initio waters. When one hydrogen bond breaks, a new hydrogen bond forms.

In the AIMD simulations for 7AI−H_2O−EFP, SA-CASSCF does not converge in one trajectory around $t \sim 45$ fs, so this trajectory was eliminated from the subsequent analyses. Among the remaining 19 trajectories examined for 7AI−H_2O−EFP, the ESHT reaction occurs in 15 trajectories, while no reaction occurs in 3 trajectories. In one trajectory, the ESHT reaction occurs once, but promptly the system returns to the normal-form region. This is an example of transition state recrossing. Figure 7 shows the time evolution of (a) the relative energy between the S_0 and S_1 states and (b) the interatomic distances along one of the 15 reactive trajectories for 7AI−H_2O−EFP. The changes of the N···H and O···H hydrogen-bond lengths become out-of-phase before the H transfer. This suggests that the ESHT of the 7AI−H_2O cluster takes place asynchronously both in the gas phase and in solution. In most of the reactive trajectories the ESHT occurs faster compared to that in the gas phase by one period of the N···H bond-length oscillation, presumably due to the thermal energy of the surrounding solvent molecules. ESHT was not observed in three trajectories, suggesting that the solvent water molecules could diminish the probability of ESHT, depending on the configuration of the surrounding water molecules.

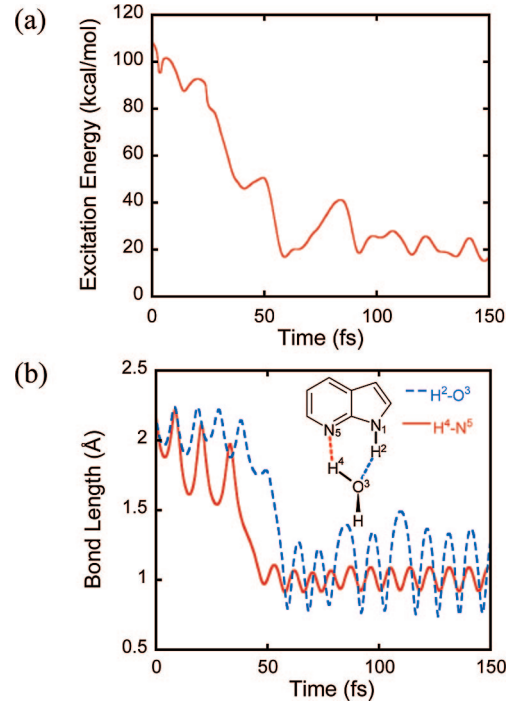

Figure 7. Time evolution of (a) the relative energy of S_0 and S_1 states and (b) the interatomic distances related to the H transfer in the AIMD simulation for 7AI−H_2O−EFP where solid and dashed lines denote changes of the $N^5\cdots H^4$ and $O^3\cdots H^2$ distances, respectively.

AIMD simulations were also carried out for 7AI−$(H_2O)_2$−EFP starting from 20 different initial conditions. The triple-H-transfer occurs in 14 trajectories, while no reaction occurs in 5 trajectories. Recrossing behavior is seen in one trajectory. Unlike 7AI−H_2O−EFP, the surrounding solvent waters affect the ESHT dynamics more significantly, resulting in different H-transfer mechanisms, depending on the initial solvent configurations. Table 2 summarizes the results of AIMD simulations for 7AI−H_2O−EFP and 7AI−$(H_2O)_2$−EFP. In 12 trajectories, the ESHT dynamics proceeds asynchronously via an H_2O−$OH^{\delta-}\cdots$7AI−$H^{\delta+}$ species in nearly half of the trajectories, while the other half of trajectories exhibit an

TABLE 2: Branching Numbers of Reaction Patterns for AIMD Simulations on 7AI−H_2O−EFP and 7AI−$(H_2O)_2$−EFP Systems

		asynchronous			
	synchronous	7AI−$H^{\delta+}$	$(H_2O)_n$−$H^{\delta+}$	recrossing	no reaction
7AI−H_2O	0	15	0	1	3
7AI−$(H_2O)_2$	2	6	6	1	5

H_2O−$H^{\delta+}$−H_2O···7$AI^{\delta-}$ species. In two trajectories, an almost-synchronous H transfer is observed. Figure 8 shows the time evolution of (a) the relative energy between the S_0 and S_1 states and (b) the interatomic distances along one of 14 reactive trajectories for 7AI−$(H_2O)_2$−EFP. The changes in the energy and the interatomic distances are similar to those in the 7AI−$(H_2O)_2$ trajectory (Figure 4, parts a and b) in some respects: (1) the relative energy shows fluctuations with a period of 11 fs in the initial stage; (2) the interatomic distances show complicated changes in the time period $t = 40$ to 60 fs with a gradual decrease of the relative energy. The fluctuations in the relative $S_0 - S_1$ energy with an approximately 20 fs cycle, observed later in the trajectory, may be caused by the vibrational motions of the 7AI ring deformation. As for 7AI−H_2O−EFP, the water molecules departing from 7AI are prevented from moving further by the surrounding EFP solvent waters.

If the transition state has some charge transfer character, polar solvents such as water should lower the activation barrier, and increase the reaction rate. The present simulations show that ESHT reactions of 7AI−H_2O and 7AI−$(H_2O)_2$ proceed via polar configurations caused by the asynchronous H transfer. A continuum model for solvation assumes that the reorientation of solvent molecules is very fast compared to the motion of solute molecule, whereas the EFP approach takes into account the reorientation process of solvent molecules explicitly. It is possible that the EFP waters do not have sufficient time to relax during the ESHT processes.

It is important to mention the limitations of the present simulation. For example, this work reports classical dynamics simulations that do not include nuclear quantum effects, such as tunneling, which could play an important role in the ESHT process. Experimentally Sakota and co-workers[18,19] suggested that quantum tunneling is a dominant mechanism for ESHT in a 7AI−(solvent) cluster in the gas phase at low temperature. One needs a quantum dynamical approach to include such quantum effects in the excited-state dynamics simulation.[52] In solution at standard thermodynamic conditions, however, the system consists of a large number of solute and solvent molecules and is expected to have sufficient energy to surpass the activation barrier upon photoexcitation. Although the present results are obtained from classical dynamics simulations, they nonetheless provide useful information related to ESHT reaction dynamics.

The foregoing 7AI−$(H_2O)_n$−EFP AIMD simulations were initiated from configurations in which one or two water molecules bridge N (six-membered ring) and H (five-membered ring) atoms of 7AI to assist the tautomerization. It is interesting to examine the number of waters that enter the 7AI hydrogen-bonded region under thermodynamic equilibrium conditions. Additional AIMD simulations were performed for 7AI + 101 EFP waters (trajectory 1) and 7AI + 102 EFP waters (trajectory 2) in the ground state using RHF/STO-3G at 300 K with a time step of 1 fs over 60 ps (60 000 steps) and with a fixed internal 7AI geometry. The initial geometries and velocities were taken from those used for the previously discussed AIMD simulations

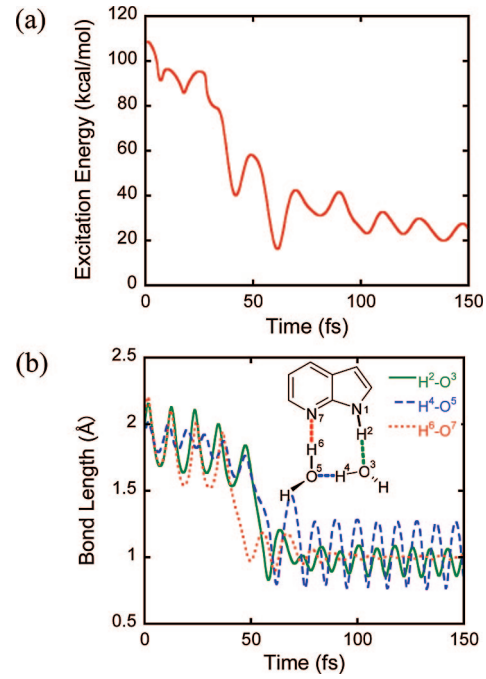

Figure 8. Time evolution of (a) the relative energy of S_0 and S_1 states and (b) the interatomic distances related to the H transfer in the AIMD simulation for 7AI−$(H_2O)_2$−EFP where solid, dashed, and dotted lines denote changes of the H^2···O^3, H^4···O^5, and H^6···N^7 distances, respectively.

on 7AI−H_2O−EFP (trajectory 1) and 7AI−$(H_2O)_2$−EFP (trajectory 2). Ab initio waters were replaced by EFP waters for these simulations. Along the trajectories, the number of configurations was counted each time an EFP water O atom entered a sphere whose center was located at the equilibrium position of the O atom of isolated 7AI−H_2O and 7AI−$(H_2O)_2$ clusters. Figure 9 illustrates the cumulative average of the probability that an O atom is inside the sphere of single-water-bridged configuration of 7AI−H_2O (case 1) and that two oxygen atoms are within the spheres of double-water-bridged configuration of 7AI−$(H_2O)_2$ (case 2). The radius of the spheres is set equal to 0.7 (Figure 9a) and 1.0 Å (Figure 9b). As seen in the figure, the spheres of the 7AI−H_2O and 7AI−$(H_2O)_2$ systems overlap appreciably; thus, when an O atom enters this overlap region and simultaneously another oxygen atom is found in the other sphere, it is counted as case 2 and not counted as case 1 in order to avoid double-counting of the configuration. One can see that converged results are obtained in case 2 for both trajectories, whereas slow convergence is seen in case 1. The relative ratio of case 2 and case 1 indicates that the single-water-bridged configurations are observed roughly twice as much as the double-water-bridged ones under the equilibrium condition of 300 K.

IV. Concluding Remarks

AIMD simulations have been performed to explore the ESHT dynamics of 7AI−$(H_2O)_n$ clusters in the gas phase and in water solution, where in the latter case the surrounding water molecules are represented by the EFP model. The AIMD simulations for the 7AI−H_2O cluster show that a hydrogen is transferred from H_2O to 7AI at $t \sim 50$ fs after the photoexcitation, and the second H transfer occurs promptly from NH on the five-membered ring (asynchronous concerted mechanism). Since the tautomer form is more stable compared to the normal form in the S_1 state, H_2O and 7AI fragments depart from each

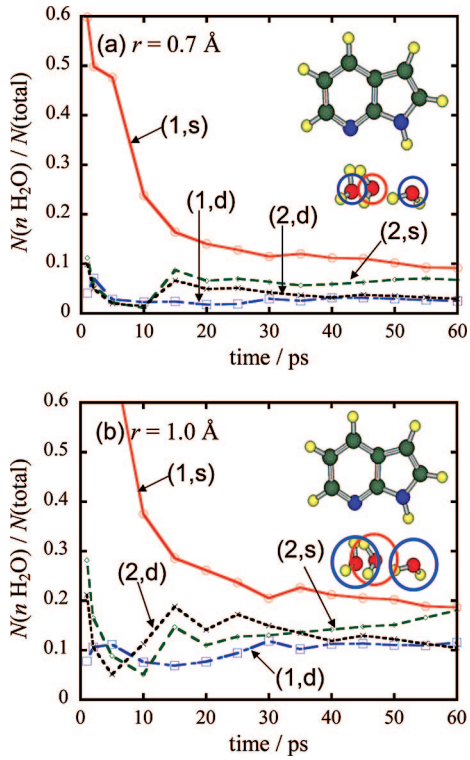

Figure 9. Cumulative average of the probability that an oxygen atom is inside the sphere of a single-water-bridged configuration of 7AI−H_2O (red circle) and that two oxygen atoms are within the spheres of double-water-bridged configuration of 7AI−$(H_2O)_2$ (blue circles), where a radius is set equal to (a) 0.7 Å and (b) 1.0 Å. (1,s) represents trajectory 1 and case 1 (single-water-bridged) and (1,d) indicates trajectory 1 and case 2 (double-water-bridged).

other just after the ESHT. For the 7AI−$(H_2O)_2$ cluster, a hydrogen on the five-membered ring moves to H_2O, and subsequently the second and third H transfers occur. This triple-H-transfer relay also occurs very quickly in a correlated way, indicating an asynchronous concerted mechanism. The relative energy between the S_0 and S_1 states after the ESHT reaction indicates the existence of a conical intersection in the region of the tautomer form. The MECI point was determined using the SA-CASSCF and CASPT2 methods. The present results suggest the possibility of a nonradiative decay after the ESHT.

To investigate the solvent effects on the ESHT dynamics in 7AI−$(H_2O)_n$ (n = 1, 2), AIMD simulations were performed for 7AI−$(H_2O)_n$ plus 100 surrounding EFP water molecules. Twenty different sets of positions and velocities were taken as the initial conditions for solvent molecules from a constant temperature MD simulation at 300 K. ESHT occurs in 15 trajectories for 7AI−H_2O−EFP and in 14 trajectories for 7AI−$(H_2O)_2$−EFP. In the former case, the ESHT reaction occurred in a similar manner to that found in the 7AI−H_2O cluster, in which the H transfer takes place asynchronously via 7AI−$H^{\delta+}\cdots OH^{\delta-}$. In contrast, in the AIMD simulations for 7AI−$(H_2O)_2$−EFP, three different mechanisms are observed. The ESHT reaction goes asynchronously through $H_2O-H^{\delta+}-H_2O\cdots$7AI$^{\delta-}$ configurations in six trajectories, whereas in six other trajectories the process goes through $H_2O-OH^{\delta-}\cdots$ 7AI−$H^{\delta+}$; in two trajectories a synchronous H transfer is observed. This result indicates that, in 7AI−$(H_2O)_2$−EFP, the ESHT dynamics is more affected by the surrounding solvent waters.

The simulations discussed here were limited to 20 trajectories for the 7AI−$(H_2O)_n$−EFP systems due to the expensive computational costs (∼100 h for each 7AI−$(H_2O)_2$−EFP trajectory on a Xeon 5160 (3.0 GHz) processor). To obtain a dynamical property, such as a reaction probability or the energy distribution of the products from statistical analyses of AIMD simulations, one would need to run many more trajectories, starting from various initial conditions. The electronic transition should be incorporated into the simulation in order to account for the possibility of nonradiative decay. This could be possible in combination with a semiclassical scheme, such as the surface-hopping algorithm.[40]

The present AIMD code has been implemented in a general ab initio program package, GAMESS.[34,35] The statistical analyses of the ESHT dynamics including electronic transition from AIMD simulations will become a tractable task in the near future.

Acknowledgment. We thank Professor H. Sekiya and Dr. K. Sakota for helpful discussions on the present reaction system. We also thank Professor T. Tahara and Dr. S Takeuchi for helpful comments on the H-transfer mechanism. The present work was supported in part by a Grant-in-Aid for Scientific Research from the Ministry of Education, Science and Culture and was supported in part by the Asian Office of Aerospace Research and Development (AOARD) and by the Air Force Office of Scientific Research.

References and Notes

(1) Arnaut, L. G.; Formosinho, S. J. *J. Photochem. Photobiol., A* **1993**, *75*, 1.
(2) Formosinho, S. J.; Arnaut, L.G. *J. Photochem. Photobiol., A* **1993**, *75*, 21.
(3) Douhal, A.; Lahmani, F.; Zewail, A. H. *Chem. Phys.* **1996**, *207*, 477.
(4) Taylor, C. A.; El-Bayoumi, M. A.; Kasha, M. *Proc. Natl. Acad. Sci. U.S.A.* **1969**, *63*, 253.
(5) Ingham, K. C.; El-Bayoumi, M. A. *J. Am. Chem. Soc.* **1974**, *96*, 1674.
(6) McMorrow, D.; Aartsma, T. J. *Chem. Phys. Lett.* **1986**, *125*, 581.
(7) Moog, R. S.; Bovino, S. C.; Simon, J. D. *J. Phys. Chem.* **1988**, *92*, 6545.
(8) Chou, P.-T.; Martinez, M. L.; Cooper, W. C.; McMorrow, D. P.; Collins, S. T.; Kasha, M. *J. Phys. Chem.* **1992**, *96*, 5203.
(9) Chapman, C. F.; Maroncelli, M. *J. Phys. Chem.* **1992**, *96*, 8430.
(10) Chen, Y.; Gai, F.; Petrich, J. W. *Chem. Phys. Lett.* **1994**, *222*, 329.
(11) Douhal, A.; Kim, S. K.; Zewail, A. H. *Nature* **1995**, *378*, 260.
(12) Smirnov, A. V.; English, D. S.; Rich, R. L.; Lane, J.; Teyton, L.; Schwabacher, A. W.; Luo, S.; Thornburg, R. W.; Petrich, J. W. *J. Phys. Chem. B* **1997**, *101*, 2758.
(13) Nakajima, A.; Hirano, M.; Hasumi, R.; Kaya, K.; Watanabe, H.; Carter, C. C.; Williamson, J. M.; Miller, T. A. *J. Phys. Chem. A* **1997**, *101*, 392.
(14) Folmer, D. E.; Wisniewski, E. S.; Stairs, J. R.; Castlman, A. W., Jr. *J. Phys. Chem. A* **2000**, *104*, 10545.
(15) Yokoyama, H.; Watanabe, H.; Omi, T.; Ishiuchi, S.; Fujii, M. *J. Phys. Chem. A* **2001**, *105*, 9366.
(16) Hara, A.; Sakota, K.; Nakagaki, M.; Sekiya, H. *Chem. Phys. Lett.* **2005**, *407*, 30.
(17) Sekiya, H.; Sakota, K. *Bull. Chem. Soc. Jpn.* **2006**, *79*, 373.
(18) Sakota, K.; Komoto, Y.; Nakagaki, M.; Ishikawa, W.; Sekiya, H. *Chem. Phys. Lett.* **2007**, *435*, 1.
(19) Sakota, K.; Inoue, N.; Komoto, Y.; Sekiya, H. *J. Phys. Chem. A* **2007**, *111*, 4596.
(20) Takeuchi, S.; Tahara, T. *Proc. Natl. Acad. Sci. U.S.A.* **2007**, *104*, 5285.
(21) Sekiya, H. Personal communication, 2008.
(22) Gordon, M. S. *J. Phys. Chem.* **1996**, *100*, 3974.
(23) Shukla, M. K.; Mishra, P. C. *Chem. Phys.* **1998**, *230*, 187.
(24) Chaban, M. G.; Gordon, M. S. *J. Phys. Chem. A* **1999**, *103*, 185.
(25) Guallar, V.; Batista, V. S.; Miller, W. H. *J. Chem. Phys.* **1999**, *110*, 9922.
(26) Fernandez-Ramos, A.; Smedarchina, Z.; Siebrand, W.; Zgierski, M. Z. *J. Chem. Phys.* **2001**, *114*, 7518.
(27) Casadesús, R.; Moreno, M.; Lluch, J. M. *Chem. Phys.* **2003**, *290*, 319.

(28) Brause, R.; Kruger, D.; Schmitt, M.; Kleinermanns, K.; Nakajima, A.; Miller, T. A. *J. Chem. Phys.* **2005**, *123*, 224311.
(29) Taketsugu, T.; Yagi, K.; Gordon, M. S. *Int. J. Quantum Chem.* **2005**, *104*, 758.
(30) Serrano-Andres, L.; Merchan, M. *Chem. Phys. Lett.* **2006**, *418*, 569.
(31) Nakano, H. *J. Chem. Phys.* **1993**, *99*, 7983.
(32) Day, P. N.; Jensen, J. H.; Gordon, M. S.; Webb, S. P.; Stevens, W. J.; Krauss, M.; Garmer, D.; Basch, H.; Cohen, D. *J. Chem. Phys.* **1996**, *105*, 1968.
(33) Gordon, M. S.; Freitag, M. A.; Bandyopadhyay, P.; Jensen, J. H.; Kairys, V.; Stevens, W. J. *J. Phys. Chem. A* **2001**, *105*, 293.
(34) Schmidt, M. W.; Baldridge, K. K.; Boatz, J. A.; Elbert, S. T.; Gordon, M. S.; Jensen, J. H.; Koseki, S.; Matsunaga, N.; Nguyen, K. A.; Su, S.; Windus, T. L.; Dupuis, M.; Montgomery, J. A. *J. Comput. Chem.* **1993**, *14*, 1347.
(35) Gordon, M. S.; Schmidt, M. W. Advances in Electronic Structure Theory: GAMESS a Decade Later. In *Theory and Applications of Computational Chemistry: The First Forty Years*; Dykstra, C. E.; Frenking, G.; Kim, K. S.; Scuseria, G. E., Eds.; Elsevier: Amsterdam, 2005; Chapter 41.
(36) Taketsugu, T.; Gordon, M. S. *J. Phys. Chem.* **1995**, *99*, 8462.
(37) Gordon, M. S.; Chaban, G.; Taketsugu, T. *J. Phys. Chem.* **1996**, *100*, 11512.
(38) Taketsugu, T.; Tajima, A.; Ishii, K.; Hirano, T. *Astrophys. J.* **2004**, *608*, 323.
(39) Kayanuma, M.; Taketsugu, T.; Ishii, K. *Chem. Phys. Lett.* **2006**, *418*, 511.
(40) Tully, J. C. *J. Chem. Phys.* **1990**, *93*, 1061.
(41) Yamamoto, H.; Matsuoka, O. *Bull. Univ. Electro−Commun.* **1992**, *5*, 23.
(42) Noro, T.; Sekiya, M.; Koga, T. *Theor. Chem. Acc.* **1997**, *98*, 25.
(43) Noro, T.; Sekiya, M.; Koga, T. *Theor. Chem. Acc.* **2003**, *109*, 85.
(44) Hockney, R. W.; Eastwood, J. W. *Computer Simulations Using Particles*; McGraw-Hill: New York, 1981.
(45) Bode, B. M.; and Gordon, M. S. *J. Mol. Graphics Modell.* **1998**, *16*, 133.
(46) Krauss, M.; Webb, S. P. *J. Chem. Phys.* **1997**, *107*, 5771.
(47) *MOLPRO*, version 2006.1, a package of ab initio programs; Werner, H.-J.; Knowles, P. J.; Lindh, R.; Manby, F. R.; Schutz, M.; and others; see: http://www.molpro.net.
(48) Celani, P.; Werner, H.-J. *J. Chem. Phys.* **2000**, *112*, 5546.
(49) Momany, F. A. *J. Phys. Chem.* **1978**, *82*, 592.
(50) Bayly, C. I.; Cieplak, P.; Cornell, W. D.; Kollman, P. A. *J. Phys. Chem.* **1993**, *97*, 10269.
(51) Ushiyama, H.; Takatsuka, K. *J. Chem. Phys.* **2001**, *115*, 5903.
(52) Martinez, T. J.; Ben-Nun, M.; Ashkenazi, G. *J. Chem. Phys.* **1996**, *104*, 2847.

JP804368P